High Capacitance Porous Ruthenium Nitride Films with High Rate Capability for Micro-Supercapacitors

Khac Huy Dinh, Grace Whang, Marielle Huve, David Troadec, Antoine Barnabé, Bruce Dunn, Pascal Roussel, Christophe Lethien

RESEARCH ARTICLE

NANO · MICRO small
www.small-journal.com

High Capacitance Porous Ruthenium Nitride Films with High Rate Capability for Micro-Supercapacitors

Khac Huy Dinh, Grace Whang, Marielle Huve, David Troadec, Antoine Barnabé, Bruce Dunn, Pascal Roussel, and Christophe Lethien**

The demand for high-performance energy storage devices to power Internet of Things applications has driven intensive research on micro-supercapacitors (MSCs). In this study, RuN films made by magnetron sputtering as an efficient electrode material for MSCs are investigated. The sputtering parameters are carefully studied in order to maximize film porosity while maintaining high electrical conductivity, enabling a fast charging process. Using a combination of advanced techniques, the relationships among the morphology, structure, and electrochemical properties of the RuN films are investigated. The films are shown to have a complex structure containing a mixture of crystallized Ru and RuN phases with an amorphous oxide layer. The combination of high electrical conductivity and pseudocapacitive charge storage properties enabled a 16 µm-thick RuN film to achieve a capacitance value of 0.8 F cm^{-2} in 1 M KOH with ultra-high rate capability.

1. Introduction

Fast charging of electrodes is a key area in the *"battery roadmap"* for the next generation of energy storage sources and microdevices that could be used to power Internet of Things devices, tiny robots, or remote sensors for healthcare, environmental, and industrial monitoring applications.[1–3] At the millimeter scale area research has shown that, although 3D lithium-based micro-batteries[4–6] can provide high areal capacities, they are limited to operating at low current densities due to their diffusion-limited charge storage process. Consequently, these devices are not optimized to sustain the high peak currents required for fast charging. However, a micro-supercapacitor (MSC), a miniaturized electrochemical capacitor, is an attractive alternative[7–10] to address the kinetic limitations and operate at much higher current densities given that the electrode materials are compatible with the fast charging process. Depending on the specific electrode material, MSCs can be classified into two main categories: electrical double-layer capacitors (EDLCs) and pseudocapacitive materials.[11] EDLCs store charge via an electrostatic charge adsorption mechanism at the electrode/electrolyte interface while pseudocapacitors store charge by fast redox reactions at the surface or sub-surface without the electrode material undergoing a phase transformation.[3,11] While the time constant of EDLC

K. H. Dinh, D. Troadec, C. Lethien
Institut d'Electronique
de Microélectronique et de Nanotechnologies
Université de Lille
CNRS
Université Polytechnique Hauts-de-France
UMR 8520 – IEMN, Lille F-59000, France
E-mail: christophe.lethien@univ-lille.fr

K. H. Dinh, M. Huve, P. Roussel
Unité de Catalyse et de Chimie du Solide (UCCS)
Université de Lille
CNRS
Centrale Lille
Université d'Artois
UMR 8181 – UCCS, Lille F-59000, France
E-mail: pascal.roussel@univ-lille.fr

K. H. Dinh, C. Lethien
Réseau sur le Stockage Electrochimique de l'Energie (RS2E)
CNRS FR 3459
33 rue Saint Leu, Amiens Cedex 80039, France

G. Whang, B. Dunn
Department of Materials Science and Engineering
University of California
Los Angeles, CA 90095, USA

A. Barnabé
CIRIMAT
Université de Toulouse
CNRS
Université Toulouse 3 Paul Sabatier
118 route de Narbonne, Toulouse Cedex 31062, France

C. Lethien
Institut Universitaire de France (IUF)
Paris 75231, France

The ORCID identification number(s) for the author(s) of this article can be found under https://doi.org/10.1002/smll.202402607

DOI: 10.1002/smll.202402607

carbon-based electrodes[12–14] is in the range of seconds (or less) and translates to good compatibility with fast charging processes, the achievable capacitances are low as they are limited by the double-layer charge storage mechanism. On the other hand, metal oxides and metal nitrides are prototypical pseudocapacitive electrode materials for MSCs which provide much higher capacitance values. The higher levels of charge storage, however, come at the expense of time constant (1–30 s), thus lowering the rate capability and the fast-charging capability. Transition metal oxides such as RuO_2 and the hydrous form of RuO_2 ($RuO_2.nH_2O$) have been widely considered for MSCs due to high electrical conductivity, long life cycle, and high capacitance (theoretical capacitance 1300 F g^{-1}).[15–19] Another example is MnO_2, which is environmentally friendly, and exhibits high capacitance (800 F g^{-1}) but suffers from low electrical conductivity.[20–22]

Transition metal nitrides (TMNs) are also considered to be promising candidates ever since the pioneering work of Conway[23] on molybdenum nitride thin films prepared by Chemical Vapor Deposition. Since then, many TMNs have been proposed as possible pseudocapacitive electrode materials for MSCs, such as binary nitrides including VN,[24–27] TiN,[28,29] NbN,[30] Mo_2N,[31] W_2N,[32] CrN[33,34] and ternary nitrides such as TiVN[35] or VWN.[36] Choi et al. reported the performance of VN nanoparticles with a high specific capacitance of 1350 F g^{-1} at 2 mV s^{-1} in 1 M KOH liquid electrolyte, with a rather large potential window (from −1.2 V to 0 V vs Hg/HgO).[37] Unfortunately, this electrochemical potential window did not allow good cycle life as it was shown later[24,38] that one must restrict the working potential window between −1 and −0.4 V versus Hg/HgO to fulfill the cycling requirements. More recently, Robert et al. achieved an areal capacitance of 1.2 F cm^{-2} at 5 mV s^{-1} in 1 M KOH with 16 µm-thick sputtered VN films in such a 0.6 V working window.[25,27] Ion implantation has also been proposed to improve the rate capability by implanting defects in VN thin films.[39] Additionally, Jrondi et al. reported very stable VN films with high cycling stability (>150 000 cycles), very low aging after 13 months, and a high areal capacitance value[26] of 1.4 F cm^{-2}. Tungsten nitride (W_2N) was also proposed as an attractive electrode material by Ouendi et al and 7.9 µm-thick sputtered W_2N films deliver up to 0.55 F cm^{-2} at 2 mV s^{-1} in 1 M KOH.[32] In most of these TMNs, the charge storage process involved the presence of an amorphous metal oxide on the surface of the metal nitride interacting with the ions coming from the aqueous electrolyte to deliver a high capacitance value associated with a pseudocapacitive process.[25,40] In summary, the TMN acts as an electronically conductive scaffold for fast electron transport enabling a fast charging process achieved by the amorphous oxide on its surface.

The thin film under vacuum deposition methods offers an exciting opportunity to unveil fundamental properties and study novel electrode materials among the many TMN candidates. Although Ruthenium nitride (RuN) is a member of the TMN family of materials, its properties and characteristics have not yet been investigated in detail. While the oxide counterpart of Ru-nitride-based material, RuO_2 is well studied as a pseudocapacitive material, only limited research has been reported for RuN.[41] The primary challenges associated with RuN are the cost of Ru and the difficulty of stabilizing the RuN phase in bulk. Due to the reduced amount of Ru material used for thin films, the cost is reduced (see Supporting Information file), enabling the utilization of this material for miniaturized devices. As for obtaining the RuN phase, it is well known that magnetron sputtering is able to stabilize metastable phases, including those of metal nitride films.[42,43] Moreover, magnetron sputtering is an industrial fabrication process that is suitable for depositing high-performance thin film electrodes for MSCs.[24,32,44–46] Several studies have shown that cycling stability was greatly improved for nitride films made by magnetron sputtering, i.e., vanadium nitride films[26] exhibited remarkable capacitance retention after 150 000 cycles as well as ternary vanadium tungsten nitride films.[36] We have recently shown the ability to synthesize RuN films with a unique nano-feather morphology using magnetron sputtering deposition.[47] To further complement and expand upon this work, it is important to elucidate how the material properties are modified and tuned by different deposition parameters in order to fabricate MSCs optimized for fast charging.

Ruthenium nitride has not been extensively studied as an electrode material for electrochemical capacitors which can be partly attributed to the difficulty in synthesizing a stable powder. However, thin film deposition methods are known for their ability to stabilize metastable phases which cannot be achieved through classical synthesis routes. In 2013, Bouhtiyya et al demonstrated that the RuN phase could be stabilized through a thin film deposition technique.[41] RuN thin film electrodes exhibited a gravimetric capacitance value of only 37 F g^{-1} between −0.5 and 0.4 V versus Hg/HgO in 1 M KOH.[41] The deposited films exhibited a face-centered cubic structure with a lattice parameter of 0.451 nm. This report contained no information about the film morphology, cycling stability, suitable working potential windows, rate capability nor charge storage mechanism. Ten years after this initial demonstration, we showed that ruthenium nitride films could be used as an efficient electrode with high capacitance and fast charge performance for electrochemical capacitors or micro-supercapacitors[47] in various aqueous electrolytes, with particularly good performance in 1 M KOH. In order to achieve the ideal and optimized nanofeather-based RuN electrodes, the sputtering deposition parameters have to be carefully selected. It is mandatory to understand the structural, chemical, morphological, electrical, and electrochemical evolution of RuN films according to the various deposition parameters. In our group, we have already shown that deposition pressure, temperature, time, gas flow rate, and the power used to bias the target are key parameters allowing us to finely tune the properties of sputtered thin films for energy storage applications.[12,24–26,32,48–50] Pressure and deposition temperature are related to ion peening and adatom diffusion processes, respectively, and both parameters can be used to tune the densification of sputtered films.[24] In sputtered TMN films, the argon to nitrogen ratio (Ar/N_2 ratio) is related to the electrical conductivity of the film, whereby the lowest nitrogen concentration leads to the highest electrical conductivity (close to that of pure metal films).[32] The gas ratio in TMNs films also plays a role in cycling stability, aging, and rate capabilities, which are key parameters for energy storage applications.[26] Target power also must be considered to achieve the expected phase.[41] Finally, the surface capacitance of an electrode made by the thin film deposition method can be increased by increasing the film thickness (i.e., the deposition time). Therefore, we investigated the effect of all the above-mentioned parameters to understand, design, and optimize RuN thin film electrodes. In

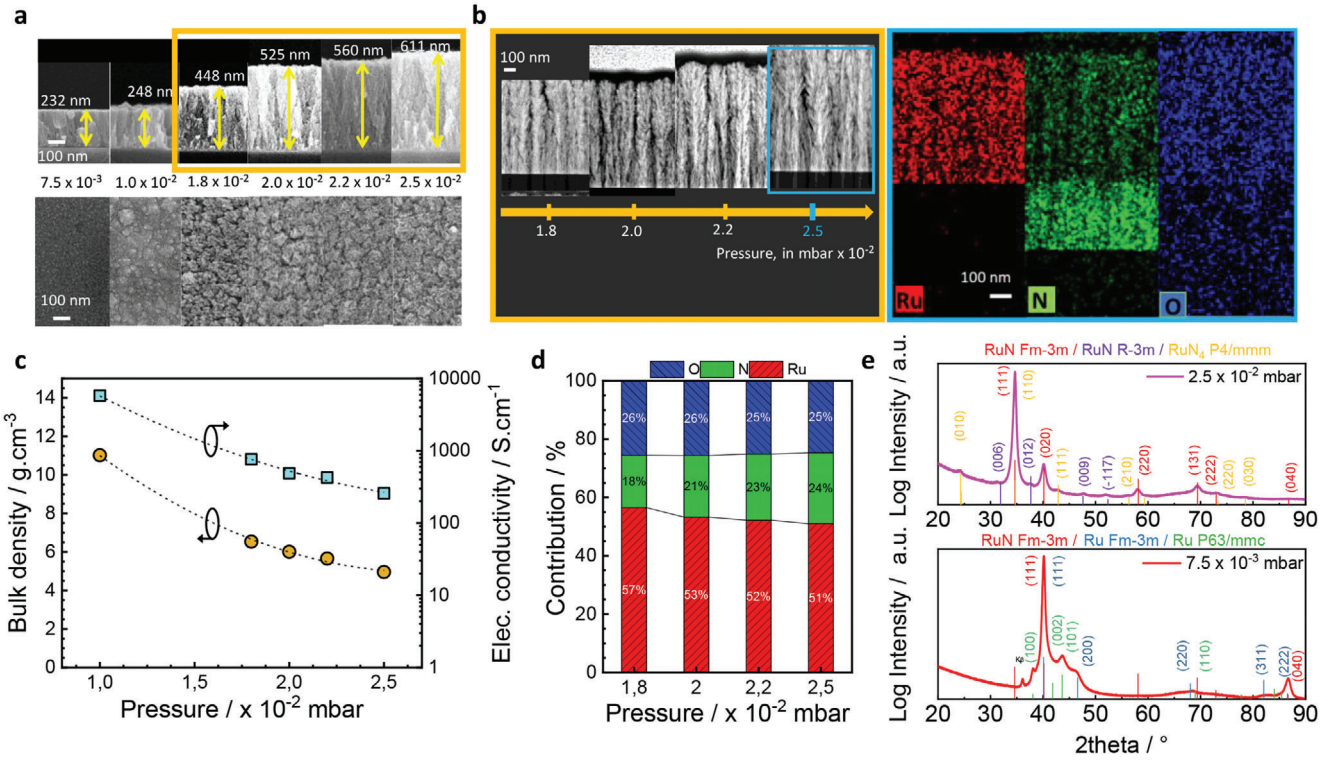

Figure 1. Morphological and structural properties of sputtered ruthenium nitride films versus the deposition pressure. a) Scanning Electron Microscope analyses (top view and cross sections) of six samples. b) Transmission Electron Microscope analyses (cross sections) of four samples. The TEM EDS analysis of the sample deposited at 2.5×10^{-2} mbar is presented in the blue box. c) Bulk density and electrical conductivity versus the pressure. d) Chemical composition as a function of operating pressures by XPS analyses. e) XRD diffractograms of the samples made at 7.5×10^{-3} and 2.5×10^{-2} mbar.

designing a miniaturized electrochemical capacitor electrode which also serves as a current collector, the thin film has to be as porous as possible while still maintaining high electrical conductivity.

In the current study, we show how to control the film morphology and composition by tuning the deposition parameters such as temperature, gas atmosphere, and deposition pressure in the magnetron sputtering process. The correlation between the morphology, structure, and electrochemical properties of the RuN films was investigated. Structural behavior of sputtered ruthenium nitride films showing a mixing of crystallized Ru and RuN phases with amorphous ruthenium oxide films are fully revealed enabling a precise understanding of the material behavior for MSC applications.

2. Results and Discussion

As mentioned above, fabricating RuN films with large porosity is necessary in order to achieve high capacitance values. The importance of the deposition pressure is described in the following section.

2.1. Effect of Deposition Pressure

For the pressure study, six Si / Si_3N_4 / RuN samples were deposited by DC magnetron sputtering at different deposition pressures while keeping the Ar/N_2 ratio, deposition temperature, power, and deposition time constant. These parameters were, respectively, 5/25 sccm, room temperature (RT), 50 W, and 30 min. The morphology of deposited samples versus the operating pressure is shown in **Figure 1a** (SEM images, cross-sections, and top views). Regardless of the deposition pressures used (in the range 7.5×10^{-3} up to 2.5×10^{-2} mbar), the sputtered films exhibit a columnar morphology. The sample morphologies fit with zone 1 of the Thornton model for metal films deposited by magnetron sputtering (i.e., a columnar morphology with voids between pillars[51]). At lower pressure (7.5×10^{-3} mbar), the RuN thickness is close to 230 nm and increases to 610 nm at higher pressures (i.e., 2.5×10^{-2} mbar). This evolution is in good agreement with previous studies on other TMN films (VN, W_2N).[24,32] The thickness of the film increases while increasing the pressure, due to the voids expanding or increasing the inter-columnar spacing.

To further investigate the evolution of the morphology versus the operating pressure, TEM analyses of the four samples deposited at the highest pressures, from 1.8×10^{-2} up to 2.5×10^{-2} mbar were conducted. FIB lamellas of Si / Si_3N_4 / RuN films were prepared and the TEM analyses shown in Figure 1b and Figures S1–S4 (Supporting Information) confirm the high porosity of the RuN films. Due to the low amount of active material inherent to thin film synthesis, it was unfortunately impossible to determine the specific surface area (in $m^2\ g^{-1}$) as usually achieved for bulk powder (BET analysis). Nevertheless, we have accurately evaluated the bulk density

of sputtered ruthenium nitride films versus the deposition pressure (Figure 1c). A significant decrease in the bulk density from ≈11 to ≈5 g cm^{-3} was observed with increasing sputter deposition pressure. From the TEM and bulk density analyses, we can conclude that the RuN films exhibited a feather-like morphology with large voids between the nanofeathers and a finer porosity inside the nanofeather. It should also be noted that the nanofeather is denser at the bottom of the film (Figures S1–S4, Supporting Information (panel a)). The electrical conductivity of the film also depends on the deposition pressure (Figure 1c) and dense films deposited at low pressure exhibited an electrical conductivity of ≈9000 S cm^{-1}, likely due to the restricted number of defects in the films. A progressive increase of the pressure induces additional porosity within the films (i.e., higher level of defects) and consequently, the electrical conductivity was lower (≈270 S cm^{-1}). This trend is similar to that recently observed for sputtered vanadium nitride films.[24,25]

TEM-EDS measurements made on the sample deposited at the highest pressure (2.5×10^{-2} mbar, Figure 1b / blue box) and for other pressures (Figures S1–S4, Supporting Information (panel b)) confirmed the film composition, highlighting the presence of ruthenium, nitrogen, and oxygen not only on the surface but also in the bulk of the RuN film. Quantification of the various elements was made from XPS analyses at the surface or sub-surface (<3 nm) of the films (Figure 1d; Figure S5a, Supporting Information). With increasing deposition pressure, the N content remains constant (25%) while Ru content decreases and O content increases. The amount of nitrogen in sputtered films varies from 18 to 24% when the deposition pressure is increased from 1.8 to 2.5×10^{-2} mbar. Moreover, the amount of ruthenium in the films decreased similarly (loss of 6%). Nevertheless, the main conclusion from these XPS analyses is the significant amount of oxygen (25%) contained in the RuN films, regardless of the operating pressure. This is corroborated by the TEM-EDS analyses reported in Figure 1b and the EDS spectrum of Figures S1–S4 (Supporting Information) (panel c) where oxygen is observed in the film not only at the surface but also in the bulk. These observations raise the question of how oxygen gets into the RuN films and we hypothesize that oxidation of the porous RuN films occurs when the samples are extracted from the sputtering equipment and get in contact to the air atmosphere. Structural analyses made by X-ray diffraction and Raman spectroscopy were employed to identify the different phases present in the film at varying deposition pressures and are depicted in Figure 1e and Figure S5b,c, (Supporting Information). The XRD patterns of the sputtered films at 2.5×10^{-2} and 7.5×10^{-3} mbar are shown in Figure 1e, while six diffractograms taken at different deposition pressures are reported in Figure S5c (Supporting Information).

The evolution of the structural behavior of sputtered RuN films with the operating pressure is quite complex. Accordingly, by fixing the gas flow ratio (5 / 25), the following conclusions can be drawn:

- At 7.5×10^{-3} and 1×10^{-2} mbar (hereafter "low pressure"), the RuN film is dense and columnar. From XRD analyses, the film contains a mixture of three phases. First, we confirm the presence of $P6_3/mmc$ hexagonal Ru metal phase (a = 2.73 and c = 4.29 Å, PDF 88–1734): the peaks at 2theta = 38.4°, 43.9°, 69.3° corresponded to (100), (101), (110) planes. Then, to explain the Bragg peaks at 2theta = 41.4°, 46.7°, 68.2°, 82° and 87°, the cubic form of Ru metal (Fm-3m, a = 3.88 Å) has to be considered: these peaks can be assigned to (111), (200), (220), (311) and (222) planes respectively.[52] Indeed, as predicted by Jain et al.[52] and observed by Kusada et al.,[53] the formation of that polymorph is stabilized by nanoscale effects.[53] Even if all the peaks are indexed with only these two phases, we cannot rule out the presence of Fm-3m cubic RuN (a = 4.48 Å) with (100) preferred orientation. Additionally, since no Raman peaks are detected (Figure S5b, Supporting Information) consequently, there is no ruthenium oxide in the film at low pressure.
- At higher pressures, (from 1.8 to 2.5×10^{-2} mbar), the sputtered films exhibit a feather-like porous morphology and are composed of mixing of Fm-3m cubic RuN (a = 4.48 Å), R-3m rhombohedral RuN (a = 2.89 and c = 17.1 Å) and P4/mmm tetragonal RuN_4 (a = 3.65 Å and c = 3.64 Å). The peaks at 34.5°, 40.1°, 58°, 69.5°, and 73° can be assigned to (111), (020), (220), (131) and (222) planes of the Fm-3m cubic RuN phase. The R-3m RuN phase is observed with peaks at 31.1°, 37.6°, 47.4°, and 52° corresponding to (006), (012), (009), and (−117) lattice planes[55]. Finally, the peaks at 2Θ = 24.4°, 34.5°, 42.8°, 73.4°, and 78.5° are related to (001), (101), (111), (202), and (221) planes of the P4/mmm RuN_4 phase.[54] Additionally, from the Raman spectra (Figure S5b, Supporting Information), we observe the formation of a ruthenium oxide phase where the associated E_g, A_{1g}, and B_{2g} peaks are measured at 505, 624 and 692 cm^{-1} respectively, which are typically observed for RuO_2.[10,55–57] The broadening of those peaks tends to demonstrate that RuO_2 is not crystallized but might be in amorphous form. As no additional peaks related to crystallized RuO_2 were evidenced on the diffractograms (Figure S5a, Supporting Information; Figure 1e), our results suggest the presence of an amorphous RuO_2 phase or crystallized nanodomains within the sputtered RuN films at high deposition pressure.

The electrochemical performance of RuN films was evaluated in 1 M KOH taking into account the working potential windows determined in our previous work.[47] The CVs of the samples at 2 mV s^{-1} in 1 M KOH are depicted in **Figure 2** while the CVs at higher scan rates (from 5 to 100 mV s^{-1}) are shown in Figure S5d (Supporting Information). Similar to the dependence of the structural properties of RuN films on deposition pressure, we observed two different behaviors. At low deposition pressures (from 7.5×10^{-3} to 1×10^{-2} mbar), the CVs have very small differences (Figure 2a, cyan and pink plots). The extracted volumetric capacitances are below 100 F cm^{-3} in both cases showing the poor electrochemical properties of RuN films deposited at low pressure. Nevertheless, due to the high electrical conductivity of the films made at low pressures, the rate capability is very high leading to similar capacitance values both at low (2 mV s^{-1}) and high scan rates (100 mV s^{-1}). At higher deposition pressures (from 1.8×10^{-2} to 2.5×10^{-2} mbar), the CVs of the four tested samples exhibited a quasi-rectangular shape indicating a (pseudo)capacitive behavior of the films.[3,58,59] For comparison purposes, the volumetric capacitance values extracted from the CV plots at different scan rates are shown in Figure 2b. At low scan rates (i.e., at 2 mV s^{-1}), the volumetric capacitance value is ≈ 580 F cm^{-3} for the sample made at 2×10^{-2} mbar. This value is roughly five times higher than that of films synthesized at low

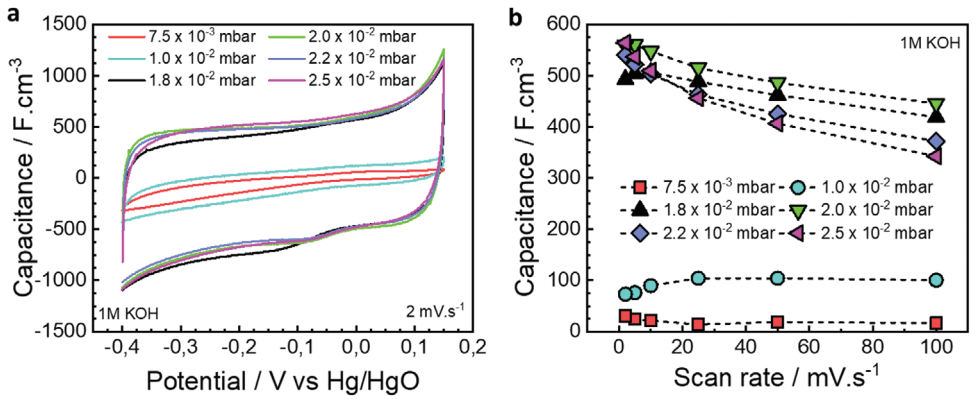

Figure 2. Electrochemical properties of sputtered ruthenium nitride films versus the deposition pressures. a) CV plots at 2 mV s^{-1} in 1 M KOH. b) Evolution of the volumetric capacitance versus the scan rates and the deposition pressures.

pressure. Taking into account a bulk density of ≈6 g cm^{-3}, the gravimetric capacitance is translated to ≈97 F g^{-1} indicating that a relatively low amount of the material is electrochemically active.

We previously showed that the films made at lower pressures are composed of crystallized Ru and RuN while the porous films made at high pressure are composed of crystallized Ru and RuN phases along with amorphous RuO_2. From the TEM-EDS analyses of the sample made at 2.5×10^{-2} mbar (and other pressures), we observed that the oxygen component is distributed throughout the entire nanofeather morphology of the film. We can conclude that the amorphous RuO_2 is the electroactive species in the RuN films made at high deposition pressure as was confirmed recently by our group.[47] We can also observe that the rate capability of RuN films is pressure-dependent (i.e., depending on the electrical conductivity and surface area from increased porosity). At 1.8×10^{-2} mbar (Figure 2b, black plot), the capacitance values at low (2 mV s^{-1}) and high scan rates (100 mV s^{-1}) were ≈500 F cm^{-3} and ≈450 F cm^{-3} respectively while the difference was higher for the sample made at 2.5×10^{-2} mbar (580 and 350 F cm^{-3} respectively, Figure 2b, pink plot).

To reach the best performance, we had to select the deposition pressure allowing both very high capacitance value and high-rate capability. Among the various tested pressures, the sample made at 2.0×10^{-2} mbar (Figure 2b, green curve) exhibited the highest capacitance value at a low scan rate (≈580 F cm^{-3}) with a high volumetric capacity at high scan rates. For that reason, the deposited pressure was set to 2.0×10^{-2} mbar for the following studies.

2.2. Effect of the Argon to Nitrogen Ratio

In addition to setting the deposition pressure of 2×10^{-2} mbar as discussed above, the other deposition parameters (deposition temperature and deposition time) used in determining the effect of the argon to nitrogen ratio were fixed at room temperature (RT) and 30 min, respectively. The argon (Ar) and nitrogen (N_2) flow rates were tuned from 0 to 30 sccm and 30–0 sccm respectively while keeping constant the total amount (Ar + N_2) of gas in the reactor at 30 sccm. The morphological, structural, and surface properties of various sputtered ruthenium nitride films versus the argon to nitrogen ratio, deposited at 2×10^{-2} mbar are depicted in **Figure 3**. SEM top view and cross section analyses for seven samples are presented in Figure 3a. The film thickness is ≈500 nm showing a columnar morphology with void and spacing within and between the columns. The surface topography issued from the SEM top view images shows a transition from pyramidal-shape films at a high nitrogen flow rate to nanostructured cauliflower-like films when the nitrogen flow rate is decreased to 15 sccm. We observe that the tuning of the gas ratio clearly influences the morphology of the RuN films which is related to the existing competition between the Ru atoms in the metallic Ru target due to argon bombardment and the ionized nitrogen atoms in the plasma and the affinity between ruthenium and nitrogen to form ruthenium metal nitride film with various composition. The addition of nitrogen in magnetron sputtering can have a significant impact on the microstructure and morphology of the deposited films.[60] Nitrogen can alter the crystallographic orientation of the deposited films, promote the growth of certain crystal planes, or induce preferred orientation. The presence of nitrogen can also influence the growth kinetics during film deposition, affecting the surface mobility of adatoms, and leading to changes in grain size and surface roughness of the deposited films. The effect of nitrogen on DC magnetron sputtering has already been demonstrated on TMN,[61] where the highest nitrogen ratio leads to the largest grain sizes, greatest roughness, highest electrical conductivity, and lowest hardness. The tuning of the gas ratio clearly modifies not only the film morphology but also has a strong influence on its structural properties. X-ray diffraction analysis depicted in Figure 3b–d enables several conclusions to be drawn, depending on the amount of nitrogen within the plasma. Three different behaviors can be observed according to the gas ratio in the sputtering chamber:

→ When the ruthenium metallic target is sputtered under a pure argon atmosphere (sample 30 / 0) at 2×10^{-2} mbar (Figure 3b), the resulting film on the substrate consists of a porous layer showing a hexagonal structure ($P6_3/mmc$) and we identify a set of Bragg peaks (at $2\Theta = 37.5°$, 42°, 44°, 57°, 69°, 82.5°, 85° and 86°) in the diffractogram corresponding to the lattice planes ((−110), (002), (101), (102), 2–10), −113), (020), (2–12) and (021)) of the $P6_3/mmc$ of the hexagonal Ru metal phase.

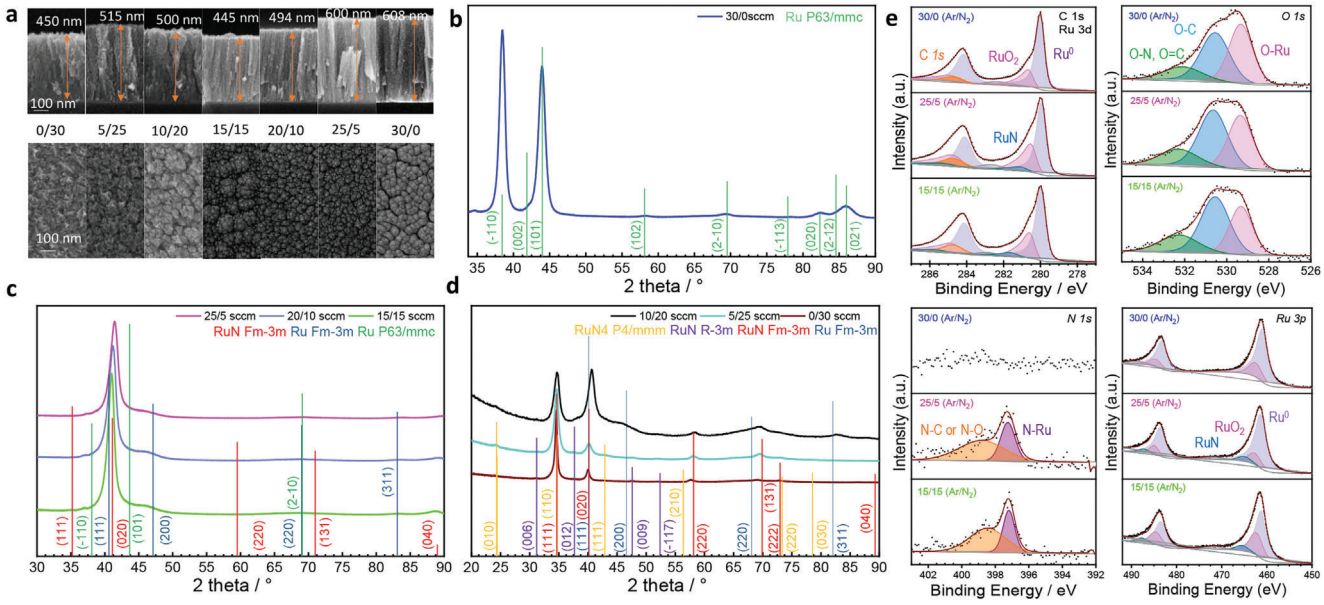

Figure 3. Morphological, structural and surface properties of sputtered ruthenium nitride films versus the argon to nitrogen ratio and deposited at 2×10^{-2} mbar. a) Top view and cross sections SEM analyses. b–d) X-Ray Diffraction analyses of various samples: b) sputtered Ru metal film. c) "Low nitrogen" content. d) "High nitrogen" content. e) Surface analyses made by XPS on metal Ru, low and high nitrogen content within the films.

→ At low nitrogen content in the total gas (15 / 15, 20 /10, and 25 / 5), i.e., when the films tend to approximate metallic behavior due to the predominance of the argon gas versus nitrogen, the XRD analyses reveal the coexistence of two Ru polymorphs (hexagonal $P6_3/mmc$ structure and Fm-3m Ru metal phase) with a cubic Fm-3m RuN nitride phase (Figure 3c and Figure S6a, Supporting Information). The hexagonal Ru phase is identified owing to the Bragg peaks at $2\Theta = 38.5°$, 43.4° and 69.5°, assigned, respectively, to the (−110), (101), and (2–10) planes of the $P6_3/mmc$ polymorph. In addition, the diffraction peaks at $2\Theta = 40.5°$, 47°, 68°, and 83.1° correspond to the (111), (200), (220) and (311) lattice planes of the cubic Fm-3m Ru metal phase. Finally, the set of diffraction peaks at $2\Theta = 35.2°$, 41°, 71°, and 89 ° are related to the cubic Fm-3m RuN phase, corresponding, respectively, to the (111), (020), (131) and (040) lattice planes. While the diffraction peaks related to both "ruthenium metal" polymorphs do not shift with the nitrogen ratio between the three samples, we clearly observe that peaks related to the cubic RuN peaks shift toward higher angles when the nitrogen flow rate is reduced from 15 to 5 sccm. For example, for the (040) plane: $2\Theta = 89°$, 89.5°, and 90.1° when the N_2 flow rate changes from 15 to 5 sccm. We note that the large full width at half maximum of the peak at 40° could in fact correspond to a set of several peaks arising from both cubic Ru and RuN phases.

→ At high nitrogen content in the total gas (Ar / N_2 = 0 / 30, 5 / 25 or 10 / 20, Figure 3d), the sputtered films are composed of a mixing of three or four phases: Fm-3m cubic Ru and RuN, R-3m rhombohedral RuN and P4/mmm tetragonal RuN_4. The four phases are identified in the 10 / 20 sample. More specifically, the Bragg peaks at $2\Theta = 40°$, 46.9°, 68.2°, and 82.8° can be assigned, respectively, to the (111), (200), (220), and (311) diffraction planes of the Fm-3m cubic Ru phase,[52] which is a Ru polymorph previously reported to form due to a nanoscale effect.[53] This cubic Fm-3m Ru phase is not observed in the two other samples (5 / 25 and 0 / 30). For the three samples, the peaks at 34.5°, 40.1°, 58°, 69.5°, 73.4°, and 87.4° can be assigned to the (111), (020), (220), (131), (222) and (040) planes of the Fm-3m cubic RuN phase. The R-3m RuN phase was proposed regarding the position of the Bragg peaks at $2\Theta = 31.2°$, 37.4°, 47.5°, and 52.2° and correspond, respectively, to the (006), (012), (009) and (−117)[54] lattice planes. Finally, the peaks at $2\Theta = 24.4°$, 34.5°, 42.8°, 73.4°, and 78.5° are attributed to the (001), (110), (111), (220) and (030) planes of the P4/mmm RuN_4 phase.[54]

From the structural analysis reported in Figure 3b–d, we observe that all the peaks can be indexed, with no unidentified phase that could be related to the presence of crystallized oxide or oxynitride phases in the films. At this point, it is important to know the chemical composition of the films and the degree of oxidation of the ruthenium. To reach this goal, XPS analyses of three different samples (30 / 0, 15 / 15, and 25 / 5) were recorded (high-resolution spectra of the Ru *3d*, C *1s*, O *1s*, N *1s*, and Ru *3p* core levels are plotted Figure 3e). Fitting the Ru component is challenging and all the data were calibrated to Ru^0 at 280 eV for the Ru *3d* core level. From the analysis of the O *1s* core level, we observe that the ratio of N_2 gas in the plasma changes the relative amounts of oxygen signals coming from RuO_2 and organic groups (C—O). Similarly, on the N *1s* core level, the incorporation of nitrogen results in the appearance of two N *1s* peaks, one corresponding to a metal nitride (RuN) and another smaller signal ≈398–400 eV, corresponding to N—O or N—C species. We also confirm that, as expected, there is no nitrogen signal in the porous metallic Ru film, sputtered in a pure argon atmosphere (30 / 0 sample). From the XPS analysis made at the Ru *3p* core level, the spectrum of

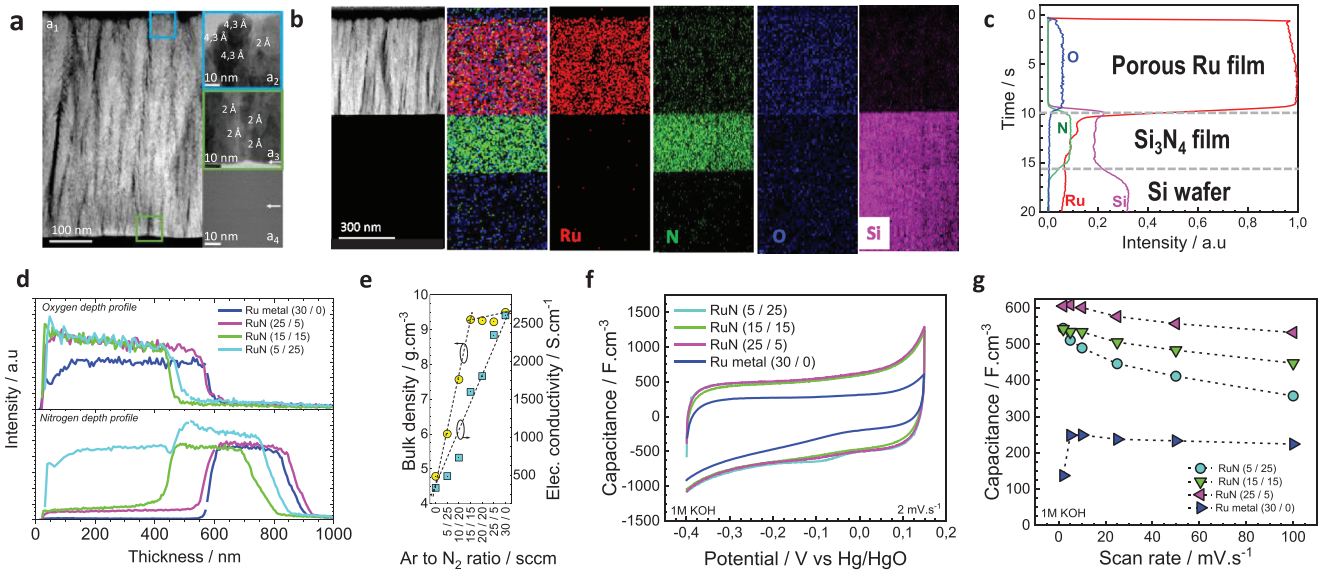

Figure 4. Structural and chemical properties of sputtered ruthenium nitride films versus the argon to nitrogen ratio and deposited at 2×10^{-2} mbar. a,b) Cross sections TEM HAADF analyses of the Ru metal film. The blue inset is focused on the top of the nanofeather while the green inset is dedicated to the Ru / Si_3N_4 interface. The white arrow shows the Si_3N_4 / Si interface and the inter-fringe distances are depicted in the insets. The HAADF image and corresponding Ru, N, O, Si EDS maps of the stacked layers is proposed to evaluate the chemical composition. c) GDOES analysis of the Ru metal films versus the etched time used to make the depth profile analyses. d) GDOES analyses focused on nitrogen and oxygen contents within the Ruthenium nitride films at various Ar/N_2 ratio. e) Electrical conductivity measurement and bulk density of various films f,g) Electrochemical properties of ruthenium nitride films in 1 M KOH.

the metallic Ru film (30 / 0 sample) exhibits two sets of peaks (Ru $3p_{1/2}$ and Ru $3p_{3/2}$) at ≈485 and ≈460 eV respectively. Each peak could be fitted with two contributions corresponding to the Ru^0 and $Ru^{IV}O_2$ elements. At the Ru $3p_{3/2}$ core level, the 1st contribution is evaluated at 461 eV and could be attributed to metallic Ru^0 while the 2nd contribution at 463.6 eV is due to $Ru^{IV}O_2$. When nitrogen is added to the plasma to form the ruthenium nitride films, we observe a 3rd contribution in the two sets of peaks at ≈465 eV and ≈487 eV respectively, which could be attributed to a nitride species RuN. Note that, in the three tested samples, we always observe the presence of oxide RuO_2 species at the surface or sub-surface of the films (after a small etching). Additionally, we also observe a significant increase in the RuO_2 quantity versus the metallic ruthenium when we increase the amount of nitrogen in the plasma. Quantification on the high-resolution spectra revealed that the RuO_2 / Ru ratio increases from (20.9% / 79.1%) for metallic Ru film to (30% / 62.6%) for the 15 / 15 sample (the last missing % corresponding to the RuN contribution). In other words, the more nitrogen in the plasma, the more oxidized the films.

While surface analyses are pertinent to determine the role of surface chemistry at the electrode/electrolyte interface for energy storage applications, it is also important to evaluate the film properties in the bulk of the material. To reach this goal, TEM analyses (on FIB lamella) and GDOES methods were carried out (**Figure 4**).

Following the same methodology used for XRD and XPS analyses, the porous metallic Ru film (30 / 0 sample) was studied by TEM and GDOES advanced characterization methods (Figure 4a–c). The TEM / HAADF images of the sputtered Ru metal film clearly exhibit a feather-like morphology (Figure 4a1). The spread of the nanofeather is more pronounced at the top of the sputtered film (Figure S6a, Supporting Information). The inset focusing at the top (Figure 4a2) and at the bottom (Figure 4a3) highlight various fringes which indicate a crystallized domain where the measured interplanar spacings (d_{001} = 4.28 Å; d_{101} = 2.05 Å and d_{100} = 2.34 Å) are in agreement with the cell parameter of the $P6_3/mmc$ hexagonal structure of Ru metal (a = 2.71 Å and c = 4.28 Å). The EDS maps (Figure 4b) of the stacked layers clearly confirm the thickness of the layers and the good quality of the interfaces (displayed in Figure 4a3,a4) without any interdiffusion between the layers. Similar observations are made for the other samples deposited 15 /15 and 25 / 5 (Figures S8 and S9, Supporting Information). The GDOES analysis of the Ru metal film is given in Figure 4c where we can show the evolution of the oxygen, nitrogen, ruthenium and silicon concentration within the Ru / Si_3N_4 / Si sample. As already observed from the TEM EDS maps and XPS surface analyses, the sputtered Ru film made at 2×10^{-2} mbar shows a significant amount of oxygen within the film.

From the GDOES analysis made on various Ru-based samples (vs the etching time), we rebuilt the depth profile as a function of film thickness for the RuN (or Ru) / Si_3N_4 stacked layers on the Si wafer. Four samples were carefully studied to check if the conclusions issued from the surface analyses (XPS) were similar when taking into account the bulk of the thin films. Oxygen and Nitrogen depth profiles of RuN (or Ru) (≈500 nm) / Si_3N_4 (≈300 nm) / Si samples are reported in Figure 4d. From the Ru metal sample, we show again the absence of nitrogen in the film and a significant amount (constant value) of oxygen from the top surface to the Ru / Si_3N_4 interface. The nitrogen depth profile of sputtered RuN films clearly shows an increase in the amount of

nitrogen as a function of the quantity of N_2 within the plasma (5 / 25 > 15 / 15 > 25 / 5). Additionally, the oxygen depth profile reveals that the nitride films are more "oxidized" than the pure Ru metal films following the results from XPS analysis. From these conclusions, we hypothesized that the electrochemical performance of the electroactive nitride films would be better than the pure metal films if the charge storage mechanism in RuN films is related to the amount of RuO_2 in the films. The amount of oxygen in the films should also influence the electrical conductivity. Consequently, we evaluated the evolution of the conductivity as a function of the argon-to-nitrogen ratio (Figure 4e). The bulk density was also measured and plotted in the same figure to highlight a densification process. From these measurements, it is clear that electrical conductivity is better (200–2600 S cm^{-1}) when the amount of nitrogen is reduced and approaches metallic behavior. This could be related to the densification process (bulk density value varies from 4.8 to 9.5 g cm^{-3}) which follows the same trend but we cannot rule out completely the role of the oxygen content in the Ru-based films.

The CV plots of the four samples cycled at 2 mV s^{-1} are depicted in Figure 4f. The CV's at other scan rates are given in Figure S6 (Supporting Information). All CVs exhibit a rectangular shape, classically observed for (pseudo)capacitive material in aqueous electrolyte. The CV of the Ru metal film (30 / 0 sample) clearly shows a lower area than the three other compositions, i.e., a lower capacitance value of the electroactive film. The CVs of the three other nitride films are very similar. The evolution of the capacitance values of the four samples with the scan-rate (from 2 to 100 mV s^{-1}), extracted from the CV plots, are given in Figure 4g. While the surface capacitance (in mF cm^{-2}) is a good metric for MSCs, a pertinent way to compare the performance of thin films consists in normalizing the surface capacitance by the film thickness, leading to volumetric capacitance (in F cm^{-3}) or normalized capacitance (in mF cm^{-2} μm^{-1}). Here we choose to report the capacitance value in F cm^{-3} taking into account that the tested Ru and RuN films have similar thicknesses (≈500 nm ± 100 nm). In this way, we compare similar thicknesses and avoid comparing a 10 nm-thick film with 100 µm-thick bulk electrodes where the nanometer-thick film could lead to unexpected capacitance values.

The volumetric capacitance of the Ru metal film stays within the range of 250 F cm^{-3} when the sweep rate changes from 5 to 100 mV s^{-1}. This response shows the high-rate capability of the metal electrode in combination with the good capacitance value arising from the (pseudo)capacitive charge storage mechanism in the nanofeather-based Ru films. When nitride films are considered, the volumetric capacitance is at least double, i.e., higher than 500 F cm^{-3} at low scan rate. This is related to the porous morphology of the nitride films and the amount of RuO_2 within the sputtered RuN layers (see XPS and GDOES analyses). The RuN sample deposited with the lowest amount of nitrogen in the plasma (25 / 5 sample) exhibits the best performance, both in terms of capacitance value at a low scan rate (≈600 F cm^{-3} at 2 mV s^{-1}) and in terms of rate capability (≈550 F cm^{-3} at 100 mV s^{-1}). This high capacitance and high rate-capability are due to the combination of several parameters: highly porous morphology at the nanoscale level (Figure 4a), very high electrical conductivity (≈2400 S cm^{-1}), and a high amount of RuO_2 species present in the total film (≈30%).

From these conclusions, the argon to nitrogen ratio was fixed to 25/5 sccm in addition to a fixed pressure of 2×10^{-2} mbar for the sputtering deposition of electroactive ruthenium nitride films. To finalize the optimization, it is necessary to check the influence of the deposition temperature and time on film properties.

2.3. Influence of the Deposition Temperature and Deposition Time on the Film Properties

To determine the influence of the deposition temperature, three samples deposited at room temperature (RT), 200 and 400 °C were compared. The results are given in **Figure 5**a–c. SEM cross sections and top view images clearly show a columnar morphology for the three films with a thickness ≈540 ± 60 nm (Figure 5a). The SEM top view analysis shows a cauliflower morphology for the RuN samples made at RT and 200 °C but there is a change of the morphology for the sample deposited at 400 °C. This modification is attributed to a densification process. The structural analysis is depicted in Figure 5b: the sample synthesized at RT is composed of different Ru and RuN phases as explained previously in regard to the "nitrogen poor" samples which produce cubic RuN Fm-3m, cubic Ru Fm-3m and hexagonal Ru $P6_3/mmc$. When the temperature is set to 200 and 400 °C, no additional phases were observed on the diffractograms. A classical crystallization process is detected as there is a significant increase in the intensity of the main diffraction peaks and a reduction of the FWHM which is correlated with grain growth (and confirmed from SEM top view imaging). The electrochemical performance of RuN films fabricated at various deposition temperatures is depicted in Figure 5c,d and Figure S10 (Supporting Information). We observe a drastic reduction of the capacitance value (600–150 F cm^{-3}) but a slight improvement of the rate-capability of the electrode with increasing sputter deposition temperature. From Figure 5e, we observe a densification process (9–12 g cm^{-3} when the deposition temperature increases from RT to 400 °C) and a significant improvement of the electrical conductivity (2500–4000 S cm^{-1}) which confirms the two previous conclusions. Consequently, the sputter deposition process provides the best electrochemical performance RuN electrodes when the deposition temperature is at room temperature.

The last parameter that we optimized is the deposition time, which is also related to the film thickness. To explore this parameter, the deposition time was varied to produce RuN films with thicknesses ranging from 0.6 to 16 µm while keeping constant all the other previously described parameters, i.e., a deposition pressure of 2×10^{-2} mbar, the argon to nitrogen ratio fixed at 25 / 5 and the temperature kept at RT. Regarding the nanofeather-like morphology of the RuN film (SEM cross sections, Figure 5f; Figure S10, Supporting Information), the stress should be minimized leading to robust electrodes for MSC's applications. Although stress was not evaluated, it is important to note that we do not observe delamination after deposition nor is there bending of the Si wafer. The film also shows strong preferred Ru (111) and RuN (020) orientation. The film preferred orientation can be modified and tuned with the deposition pressure[12] as well as the gas ratio.[62] Such orientation could affect the charge transport,

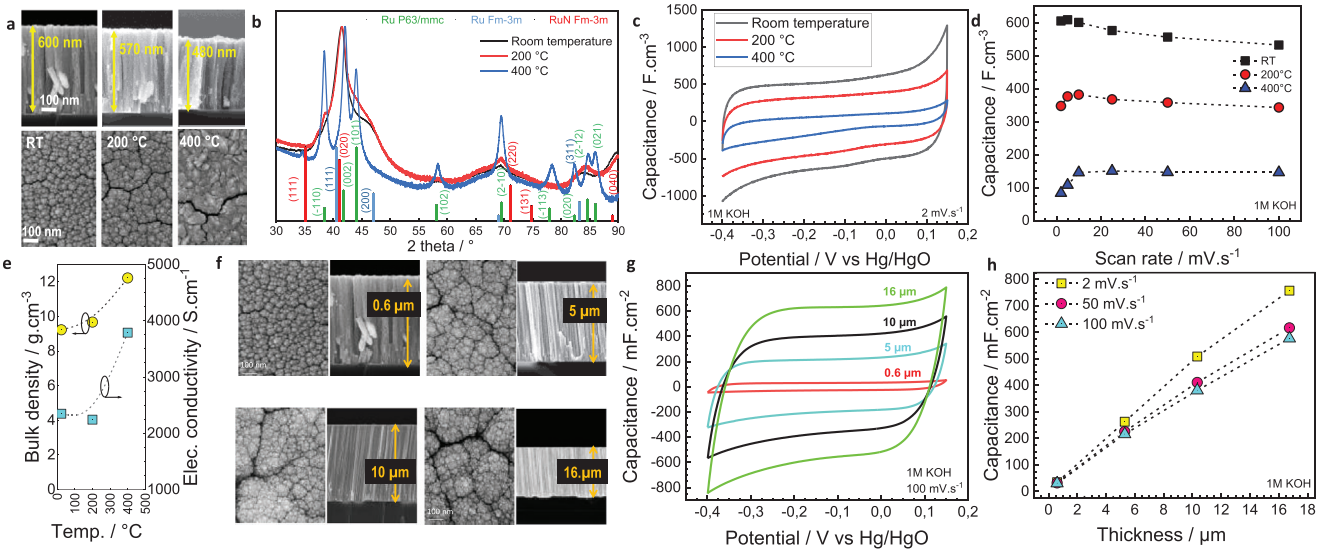

Figure 5. Structural, electrical, morphological, and electrochemical properties of sputtered ruthenium nitride films versus the temperature and the thickness while keeping fixed the pressure (2×10^{-2} mbar) and the Argon to Nitrogen ratio (25 / 5). a) Cross-section TEM analyses of the RuN films as a function of temperature. b) X-Ray Diffraction analyses of the sputtered RuN films. c,d) Electrochemical properties of the RuN as a function of temperature in 1 M KOH. e) Electrical conductivity measurement and bulk density of various films g,h) Electrochemical properties in 1 M KOH of ruthenium nitride films as a function of film thickness at 100 mV s^{-1} g) and various scan rates h) showing the high rate capability of the RuN electrode for A-MSC.

charge/discharge rate of the film[48,63,64] and overall, the electrochemical performance of the film.

The electrochemical performance of the films (Figure 5g,h) was measured in 1 M KOH as a function of film thickness at various scan rates (from 2 to 100 mV s^{-1}). The CV plots at 100 mV s^{-1} are depicted in **Figure 6**g and the CVs at other scan rates are presented in Figure S10, (Supporting Information). Regarding the shape of the CV, the high rate capability of RuN electrodes (cycling time <6 s) was observed irrespective of the thickness due to the porous morphology of the electrode, the presence of amorphous RuO_2 species, and the high electrical conductivity of the RuN scaffold. The capacitance values were extracted from the CV and plots at various scan rates (2, 50 and 100 mV s^{-1}). From the capacitance versus thickness plot in Figure 5h, the linear profile observed at all scan rates suggests that within the scan rates tested, there is no limitation of the ion diffusion / electron transfer within the thin and thick electrodes. The 16 µm-thick RuN film deposited by magnetron sputtering using the optimized conditions identified in our studies reaches a remarkably high capacitance value close to 800 mF cm^{-2}. This values represents a significant improvement compared to other TMN thin film electrodes (550 mF cm^{-2} for 16 µm-thick W_2N,[32] 220 mF cm^{-2} for 17.4 µm-thick Nb_4N_5,[30] 40 mF cm^{-2} for 1.1 µm-thick CrN[65]). The optimized RuN films developed here can clearly operate as a positive electrode between −0.4 and 0.15 V versus Hg/HgO for MSC operating in 1 M KOH electrolyte.

By the way, it was recently shown[10] that the VN and RuO_2 pseudocapacitive materials are complementary electrodes in an asymmetric configuration for micro-supercapacitor (A- MSC) but the hydrous-RuO_2 film was the limiting electrode due to the low thickness of the electrodeposited material (≈700 nm). To maximize the performance, the pseudocapacitive films can be either deposited on a 3D scaffold[1,19,66] or the thickness has to be improved while maintaining the high electrical conductivity of the electrode. The Magnetron sputtering deposition method is not suitable to produce step conformal film on the 3D scaffold and the thickness of the electrode was increased. Consequently, thick RuN films (≥5 µm) can be paired with VN in order to increase the total amount of electroactive material within the electrode. The RuN film is considered the positive electrode (−0.4 V to 0.15 V vs Hg/HgO) while the VN film[25,39] is the negative one and operates from −1.0 V to −0.4 V versus Hg/HgO. The complementary working window potential of VN and RuN electrodes can be utilized to fabricate VN // RuN A-MSC with a cell voltage of up to 1.15 V in 1 M KOH electrolyte (Figure 6). The Nyquist plot, evaluated in 1 M KOH by electrochemical impedance spectroscopy, is depicted in Figure 6a and clearly shows the capacitive behavior of the A-MSC with the vertical line response at low frequency.

To balance the charge between the VN and RuN electrodes (to avoid charge limitation), 10.3 µm-thick RuN film was paired with 5.1 µm-thick VN film which provides the same charge of 0.28 C cm^{-2} at a scan rate of 2 mV s^{-1}. The cell voltage of the VN // RuN A-MSC is ≈1.15 V. The CV plots (Figure 6b) at various scan rates from 2 to 100 mV s^{-1} of the A-MSC are in agreement with the classical rectangular CV shape from an electrochemical capacitor or MSC made from capacitive or pseudocapacitive materials.[3,59,67] The long-term cycling properties of VN // RuN A-MSC were investigated in 1 M KOH: 80% of the initial capacitance value is maintained after 10 000 cycles (Figure 6c).

3. Conclusion

We investigated RuN films as an efficient electrode material for MSCs or ECs. The DC magnetron sputtering method was employed to fabricate RuN films. The morphology and structure are directly related to the electrochemical properties of the film which, in turn, are well known to be influenced by the sputtering parameters (i.e., pressure, argon to nitrogen ratio,

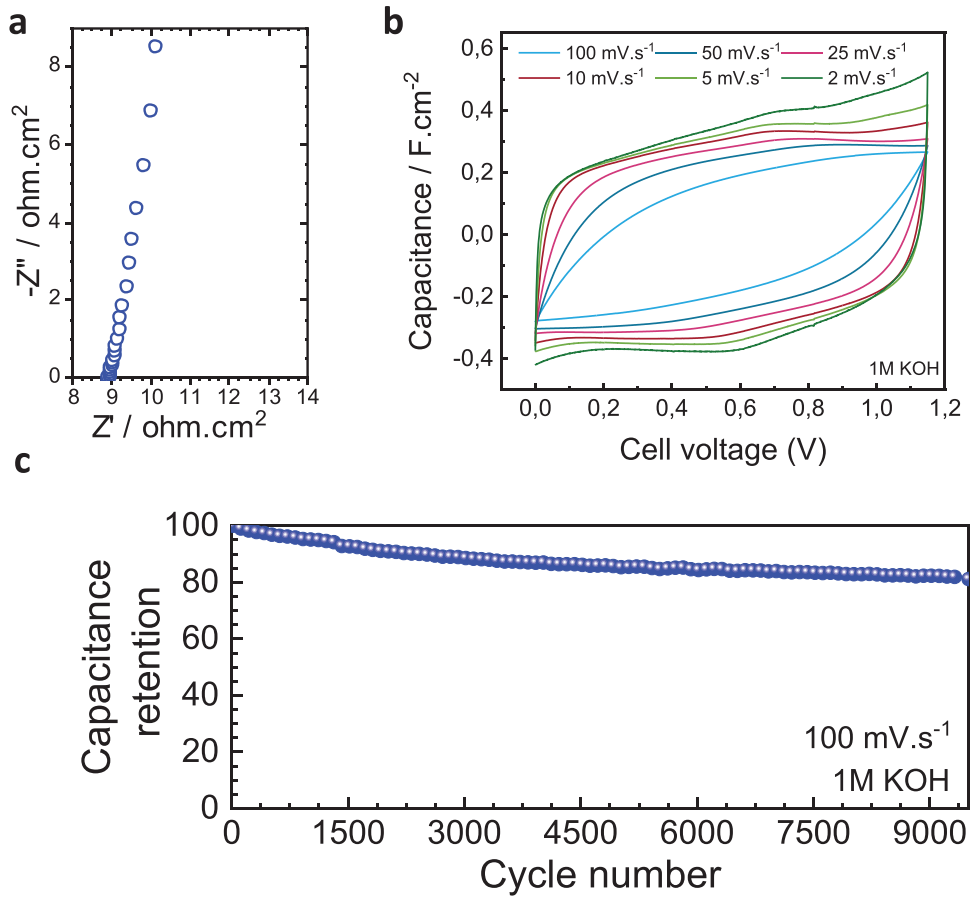

Figure 6. Electrochemical performance of asymmetric VN // RuN MSC in 1 M KOH. a) Nyquist plot of the MSC in 1 M KOH. b) CV plots at various scan rates. c) Capacitance retention during 10 000 cycles in 1 M KOH.

temperature). Therefore, we carefully studied these parameters to establish the optimal conditions for synthesizing RuN films. The deposition parameters of 2.0×10^{-2} mbar for pressure, 25/5 sccm for Ar/N_2 gas ratio, and a temperature of 25 °C (RT) led to the RuN films with the best electrochemical properties. By using a series of complimentary characterization techniques (i.e., XRD, TEM, EDS, XPS, GDOES), we were able to understand the complexity of the film composed of various crystallized Ru and RuN species and amorphous RuO_2. The amount of RuO_2 in the films deposited on a high electrical conductivity RuN/Ru scaffold plays a crucial role in determining electrochemical performance. We demonstrate fast charging of a high-capacity film using a 16 µm-thick RuN electrode that operates at a high scan rate (0.1 V s^{-1}) and possesses high areal and volumetric capacitance values of 0.8 F cm^{-2} and 500 F cm^{-3}, respectively.

4. Experimental Section

Sputtering Deposition of RuN Films: To prevent the etching of the Si substrate by the aqueous electrolyte (1 M KOH) used in electrochemical experiments, a highly dense layer of Si_3N_4 (300 nm) was deposited by low-pressure chemical vapor deposition (LP CVD) at 800 °C (flow rates: 60 sccm for NH_3 and 20 sccm for SiH_2Cl_2) on the Si wafer. Then RuN was deposited on the substrate by direct current magnetron sputtering (DC MS) from a pure 4-inch ruthenium target (99.9%) using a CT200 Alliance Concept reactor under an Ar / N_2 atmosphere. Before the deposition, the pressure was kept below 10^{-6} mbar and the target-substrate distance was fixed at 6 cm. The deposition parameters (pressure, Argon to Nitrogen ratio, deposition time) were tuned during this study in order to fabricate the porous thin film electrodes required for high-rate charge storage.

Structural and Morphological Characterizations of the RuN Thin Films: Electrical measurements were performed with eddy currents using Semilab WT 2000PVN contactless equipment. TEM measurements were conducted on a S/TEM FEI TITAN Themis 300 equipped with a probe corrector for a resolution of 0.6 Å in STEM mode, an electron monochromator for an energy resolution of 140 meV, and a Super-X quad EDS detector for elemental analysis. The microscope had several annular detectors for imaging, and a postcolumn GATAN Quantum ERS/966 GIF operating a dual EELS mode.

For the STEM experiment, a spot-size 9, a convergence semi-angle of 20.5 mrad, and a beam current of between 50 and 100 nA were used along with a HAADF detector collection angle of between 50 and 200 mrad. Prior to this, the sample had been thinned and mounted on a TEM copper grid using a FIB / SEM to meet the requirements for TEM observation. The STEM-EELS experiment was performed in spectrum imaging mode with a dispersion of 0.25 eV ch^{-1}, 1.5 nm step, and a 0.05 s dwell time, thereby simultaneously acquiring the low-loss and core-loss energy range and the collection angle, respectively, at 49 mrad. The spectral images were later realigned to compensate for drift in energy by the zero-loss peak.

The morphology of the RuN thin film was determined by using a Zeiss Ultra 55 scanning electron microscope (SEM cross-section and top view analyses) and a microbalance (Mettler Toledo XP6U) was used to determine the density of the films (in g cm^{-3}).

The structural properties were studied using a 9 kW rotated anode Rigaku Smartlab diffractometer in Bragg-Brentano geometry, delivering Cu Kα radiation (λ = 1.5418 Å). A 4° offset of the substrate was applied to avoid detector saturation due to the high intensity of the (100) silicon peak. A LabRAM HR800 Raman spectrometer (HORIBA Scientific, Jobin-Yvon) was employed to collect Raman spectra.

The Glow Discharge Optical Emission Spectroscopy (GDOES) experiments were carried out using a HORIBA Profiler 2 at the Centre de microcaractérisation Raimond Castaing (Toulouse, France).

The X-ray photoelectron spectroscopy (XPS) experiments were carried out using a Kratos Axis Ultra DLD with a monochromatic Al Kα radiation source using a voltage of 10 kV and emission current of 10 mA at the University of California, Los Angeles (Los Angeles, USA). The data was processed using CasaXPS software and a Shirley background was used for the analysis.

Electrochemical Analyses: The electrochemical properties of RuN electrode were measured in a three-electrode configuration in 1 M KOH aqueous electrolytes. The RuN film, a platinum wire, and a Hg/HgO act as the working electrode (WE), the counter electrode, and the reference electrode, respectively. Cyclic voltammetry (CV), galvanostatic charge and discharge (GCD) plots, and electrochemical impedance spectroscopy (EIS) were carried out on a Biologic VMP3 potentiostat/galvanostat equipment. For the EIS experiments, measurements were made at open circuit voltage over the frequency range from 100 kHz to 100 mHz with an amplitude of 50 mV rms.

The surface capacitance (or "areal" capacitance) measured by CV techniques was calculated by normalizing the capacitance (in mF) according to the tested area (footprint area in cm^{-2}), thereby furnishing real capacitance values in mF cm^{-2}. The specific capacitance (C, mF cm^{-2}) was calculated according to the following equation:

$$C = \frac{\int Idt}{S\Delta V} \quad (1)$$

where I, S, and ΔV are the current (mA), footprint area (0.407 cm^2), and cell voltage (V), respectively. The volumetric capacitance (F cm^{-3}) was obtained by dividing the areal capacitance by the film thickness, evaluated via SEM in cross sections.

Supporting Information

Supporting Information is available from the Wiley Online Library or from the author.

Acknowledgements

This project received funding from the European Union's Horizon 2020 research and innovation program under the Marie Sklodowska-Curie grant agreement no. 847568. The authors thank the French National Research Agency (STORE-EX Labex Project ANR-10-LABX-76-01 and ARTEMIS ANR project). The French RENATECH network and the University of Lille are greatly acknowledged for supporting the Center of MicroNanoFabrication (CMNF) facility from IEMN. The authors also want to thank the Department of Materials Science and Engineering (UCLA) for the use of XPS facilities, Centre de Microcaractérisation Raimond Castaing (Toulouse, France) for the use of GDOES facilities, and Chevreul Institute (FR 2638) for funding XRD and TEM facilities. This work received funding from the CPER Hauts de France project IMITECH and MEL. Partial support at UCLA was provided by the Office of Naval Research (N00014-23-1-2667).

Conflict of Interest

The authors declare no conflict of interest.

Author Contributions

K.H.D. performed methodology, investigation, formal analysis, visualization, wrote, reviewed, and edited—original draft, resources, data curation. D.T. performed FIB preparation for TEM analyses. A.B. performed an investigation (GDOES). M.H. performed formal analysis, and investigation (TEM). G.W. and B.D. performed formal analysis and investigation (XPS). P.R. performed resources, conceptualization, methodology, validation, wrote, reviewed, and edited—original draft, Supervision, funding acquisition, and project administration. C.L. performed resources, conceptualization, methodology, validation, wrote, reviewed, and edited—original draft, supervision, funding acquisition, and project administration.

Data Availability Statement

The data that support the findings of this study are available from the corresponding author upon reasonable request.

Keywords

micro-supercapacitors, pseudocapacitive, ruthenium nitride

Received: April 2, 2024
Revised: May 21, 2024
Published online:

[1] C. Lethien, J. Le Bideau, T. Brousse, *Energy Environ. Sci.* **2019**, *12*, 96.
[2] M. Zhu, O. G. Schmidt, *Nature* **2021**, *589*, 195.
[3] P. Simon, Y. Gogotsi, *Nat. Mater.* **2020**, *19*, 1151.
[4] J. I. Hur, L. C. Smith, B. Dunn, *Joule* **2018**, *2*, 1187.
[5] M. Létiche, E. Eustache, J. Freixas, A. Demortière, V. De Andrade, L. Morgenroth, P. Tilmant, F. Vaurette, D. Troadec, P. Roussel, T. Brousse, C. Lethien, *Adv. Energy Mater.* **2017**, *7*, 1601402.
[6] A. Pearse, T. Schmitt, E. Sahadeo, D. M. Stewart, A. Kozen, K. Gerasopoulos, A. A. Talin, S. B. Lee, G. W. Rubloff, K. E. Gregorczyk, *ACS Nano* **2018**, *12*, 4286.
[7] P. Huang, C. Lethien, S. Pinaud, K. Brousse, R. Laloo, V. Turq, M. Respaud, A. Demortière, B. Daffos, P. L. Taberna, B. Chaudret, Y. Gogotsi, P. Simon, *Science (80-.)*. **2016**, *351*, 691.
[8] Q. Jiang, N. Kurra, M. Alhabeb, Y. Gogotsi, H. N. Alshareef, *Adv. Energy Mater.* **2018**, *8*, 1703043.
[9] E. Eustache, C. Douard, A. Demortière, V. De Andrade, M. Brachet, J. Le Bideau, T. Brousse, C. Lethien, *Adv. Mater. Technol.* **2017**, *2*, 1700126.
[10] B. Asbani, K. Robert, P. Roussel, T. Brousse, C. Lethien, *Energy Storage Mater.* **2021**, *37*, 207.
[11] Y. Shao, M. F. El-Kady, J. Sun, Y. Li, Q. Zhang, M. Zhu, H. Wang, B. Dunn, R. B. Kaner, *Chem. Rev.* **2018**, *118*, 9233.
[12] M. Létiche, K. Brousse, A. Demortière, P. Huang, B. Daffos, S. Pinaud, M. Respaud, B. Chaudret, P. Roussel, L. Buchaillot, P. L. Taberna, P. Simon, C. Lethien, *Adv. Funct. Mater.* **2017**, *27*, 160813.
[13] Y. Zhu, S. Murali, M. D. Stoller, K. J. Ganesh, W. Cai, P. J. Ferreira, A. Pirkle, R. M. Wallace, K. A. Cychosz, M. Thommes, D. Su, E. A. Stach, R. S. Ruoff, *Science (80-.)*. **2011**, *332*, 1537.
[14] D. Pech, M. Brunet, H. Durou, P. Huang, V. Mochalin, Y. Gogotsi, P.-L. Taberna, P. Simon, *Nat. Nanotechnol.* **2010**, *5*, 651.
[15] D. A. McKeown, P. L. Hagans, L. P. L. Carette, A. E. Russell, K. E. Swider, D. R. Rolison, *J. Phys. Chem. B* **1999**, *103*, 4825.
[16] J. W. Long, K. E. Swider, C. I. Merzbacher, D. R. Rolison, *Langmuir* **1999**, *15*, 780.
[17] B. E. Conway, V. Birss, J. Wojtowicz, *J. Power Sources* **1997**, *66*, 1.

[18] W. Sugimoto, H. Iwata, K. Yokoshima, Y. Murakami, Y. Takasu, *J. Phys. Chem. B* **2005**, *109*, 7330.
[19] B. Asbani, G. Buvat, J. Freixas, M. Huvé, D. Troadec, P. Roussel, T. Brousse, C. Lethien, *Energy Storage Mater.* **2021**, *42*, 259.
[20] M. Toupin, T. Brousse, D. Bélanger, *Chem. Mater.* **2004**, *16*, 3184.
[21] E. Eustache, C. Douard, R. Retoux, C. Lethien, T. Brousse, *Adv. Energy Mater.* **2015**, *5*, 3.
[22] M. Dupont, A. F. Hollenkamp, S. W. Donne, *Electrochim. Acta* **2013**, *104*, 140.
[23] T.-C. Liu, W. G. Pell, B. E. Conway, S. L. Roberson, *J. Electrochem. Soc.* **1998**, *145*, 1882.
[24] K. Robert, C. Douard, A. Demortière, F. Blanchard, P. Roussel, T. Brousse, C. Lethien, *Adv. Mater. Technol.* **2018**, *3*, 1800036.
[25] K. Robert, D. Stiévenard, D. Deresmes, C. Douard, A. Iadecola, D. Troadec, P. Simon, N. Nuns, M. Marinova, M. Huvé, P. Roussel, T. Brousse, C. Lethien, *Energy Environ. Sci.* **2020**, *13*, 949.
[26] A. Jrondi, G. Buvat, F. D. La Pena, M. Marinova, M. Huvé, T. Brousse, P. Roussel, C. Lethien, *Adv. Energy Mater.* **2023**, *2203462*, 1.
[27] C. Choi, K. Robert, G. Whang, P. Roussel, C. Lethien, B. Dunn, *Joule* **2021**, *5*, 2466.
[28] A. Achour, R. L. Porto, M. A. Soussou, M. Islam, M. Boujtita, K. A. Aissa, L. Le Brizoual, A. Djouadi, T. Brousse, *J. Power Sources* **2015**, *300*, 525.
[29] J. Freixas, E. Eustache, P. Roussel, C. Brillard, D. Deresmes, N. Nuns, N. Rolland, T. Brousse, C. Lethien, *J. Electrochem. Soc.* **2015**, *162*, A493.
[30] H. Cui, G. Zhu, X. Liu, F. Liu, Y. Xie, C. Yang, T. Lin, H. Gu, F. Huang, *Adv. Sci.* **2015**, *2*, 1500126.
[31] L. Chen, C. Liu, Z. Zhang, *Electrochim. Acta* **2017**, *245*, 237.
[32] S. Ouendi, K. Robert, D. Stievenard, T. Brousse, P. Roussel, C. Lethien, *Energy Storage Mater.* **2019**, *20*, 243.
[33] M. Arif, A. Sanger, A. Singh, *Mater. Lett.* **2018**, *220*, 213.
[34] E. Haye, A. Achour, A. Guerra, F. Moulaï, T. Hadjersi, R. Boukherroub, A. Panepinto, T. Brousse, J. J. Pireaux, S. Lucas, *Electrochim. Acta* **2019**, *324*, 134890.
[35] A. Achour, R. Lucio-Porto, M. Chaker, A. Arman, A. Ahmadpourian, M. A. Soussou, M. Boujtita, L. Le Brizoual, M. A. Djouadi, T. Brousse, *Electrochem. Commun.* **2017**, *77*, 40.
[36] K. H. Dinh, K. Robert, J. Thuriot-Roukos, M. Huvé, P. Simon, D. Troadec, C. Lethien, P. Roussel, *Chem. Mater.* **2023**, *35*, 8654.
[37] D. Choi, G. E. Blomgren, P. N. Kumta, *Adv. Mater.* **2006**, *18*, 1178.
[38] A. Morel, Y. Borjon-Piron, R. L. Porto, T. Brousse, D. Bélanger, *J. Electrochem. Soc.* **2016**, *163*, A1077.
[39] E. L. Calvez, D. Yarekha, L. Fugère, K. Robert, M. Huvé, M. Marinova, O. Crosnier, C. Lethien, T. Brousse, *Electrochem. Commun.* **2021**, *125*, 107016.
[40] A. Djire, P. Pande, A. Deb, J. B. Siegel, O. T. Ajenifujah, L. He, A. E. Sleightholme, P. G. Rasmussen, L. T. Thompson, *Nano Energy* **2019**, *60*, 72.
[41] S. Bouhtiyya, R. Lucio Porto, B. Laïk, P. Boulet, F. Capon, J. P. Pereira-Ramos, T. Brousse, J. F. Pierson, *Scr. Mater.* **2013**, *68*, 659.
[42] W. Sun, C. J. Bartel, E. Arca, S. R. Bauers, B. Matthews, B. Orvañanos, B. R. Chen, M. F. Toney, L. T. Schelhas, W. Tumas, J. Tate, A. Zakutayev, S. Lany, A. M. Holder, G. Ceder, *Nat. Mater.* **2019**, *18*, 732.
[43] E. Arca, S. Lany, J. D. Perkins, C. Bartel, J. Mangum, W. Sun, A. Holder, G. Ceder, B. Gorman, G. Teeter, W. Tumas, A. Zakutayev, *J. Am. Chem. Soc.* **2018**, *140*, 4293.
[44] B. Wei, H. Liang, D. Zhang, Z. Wu, Z. Qi, Z. Wang, *J. Mater. Chem. A* **2017**, *5*, 2844.
[45] Z. Gao, Z. Wu, S. Zhao, T. Zhang, Q. Wang, *Mater. Lett.* **2019**, *235*, 148.
[46] S. Wang, L. Zhang, C. Sun, Y. Shao, Y. Wu, J. Lv, X. Hao, *Adv. Mater.* **2016**, *28*, 3768.
[47] H. Dinh Khac, G. Whang, A. Iadecola, H. Makhlouf, A. Barnabé, A. Teurtrie, M. Marinova, M. Huvé, I. Roch-Jeune, C. Douard, T. Brousse, B. Dunn, P. Roussel, C. Lethien, *Nat. Mater.* **2024**, *23*, 670.
[48] M. Létiche, M. Hallot, M. Huvé, T. Brousse, P. Roussel, C. Lethien, *Chem. Mater.* **2017**, *29*, 6044.
[49] C. Arico, S. Ouendi, P. L. Taberna, P. Roussel, P. Simon, C. Lethien, *ACS Nano* **2019**, *13*, 5826.
[50] G. Buvat, A. Iadecola, F. Blanchard, T. Brousse, P. Roussel, C. Lethien, *J. Electrochem. Soc.* **2021**, *168*, 030524.
[51] J. A. Thornton, *Model. Opt. Thin Film.* **1988**, *0821*, 95.
[52] A. Jain, S. P. Ong, G. Hautier, W. Chen, W. D. Richards, S. Dacek, S. Cholia, D. Gunter, D. Skinner, G. Ceder, K. A. Persson, *APL Mater.* **2013**, *1*, 011002.
[53] K. Kusada, H. Kobayashi, T. Yamamoto, S. Matsumura, N. Sumi, K. Sato, K. Nagaoka, Y. Kubota, H. Kitagawa, *J. Am. Chem. Soc.* **2013**, *135*, 5493.
[54] Y. Zhang, L. Wu, B. Wan, Y. Lin, Q. Hu, Y. Zhao, R. Gao, Z. Li, J. Zhang, H. Gou, *Sci. Rep.* **2016**, *6*, 33506.
[55] H. C. Jo, K. M. Kim, H. Cheong, S. H. Lee, S. K. Deb, *Electrochem. Solid-State Lett.* **2005**, *8*, E39.
[56] P. C. Liao, C. S. Chen, W. S. Ho, Y. S. Huang, K. K. Tiong, *Thin Solid Films* **1997**, *301*, 7.
[57] L. jian Meng, V. Teixeira, M. P. Dos Santos, *Thin Solid Films* **2003**, *442*, 93.
[58] S. Fleischmann, J. B. Mitchell, R. Wang, C. Zhan, D. E. Jiang, V. Presser, V. Augustyn, *Chem. Rev.* **2020**, *120*, 6738.
[59] T. Brousse, D. Belanger, J. W. Long, *J. Electrochem. Soc.* **2015**, *162*, A5185.
[60] J. Musil, J. Vlček, *Mater. Chem. Phys.* **1998**, *54*, 116.
[61] D. Dastan, K. Shan, A. Jafari, F. Gity, X. T. Yin, Z. Shi, N. D. Alharbi, B. A. Reshi, W. Fu, Ş. Ţălu, L. Aljerf, H. Garmestani, L. Ansari, *Appl. Phys. A Mater. Sci. Process.* **2022**, *128*, 400.
[62] H. K. Kim, T. Y. Seong, J. H. Lim, W. Cho, Y. S. Yoon, *J. Power Sources* **2001**, *102*, 167.
[63] X. Liu, P. Carvalho, M. N. Getz, T. Norby, A. Chatzitakis, *J. Phys. Chem. C* **2019**, *123*, 21931.
[64] M. Hallot, A. Demortière, P. Roussel, C. Lethien, *Energy Storage Mater.* **2018**, *15*, 396.
[65] B. Wei, G. Mei, H. Liang, Z. Qi, D. Zhang, H. Shen, Z. Wang, *J. Power Sources* **2018**, *385*, 39.
[66] T. Guillemin, C. Douard, K. Robert, B. Asbani, C. Lethien, T. Brousse, J. Le Bideau, *Energy Storage Mater.* **2022**, *50*, 606.
[67] K. H. Dinh, P. Roussel, C. Lethien, *ACS Omega* **2023**, *8*, 8977.